Typhoon-Induced Ground Deformation

Maxime Mouyen, A. Canitano, B. F. Chao, Y.-J. Hsü, Philippe Steer, Laurent Longuevergne, J.-P. Boy

AGU PUBLICATIONS

Geophysical Research Letters

RESEARCH LETTER
10.1002/2017GL075615

Key Points:
- Analyze 72 typhoon-induced deformation signals at up to seven strainmeters for 10 years and 31 typhoons
- Quantify the contribution of air pressure, nontidal ocean loading, and rainfalls on the deformation
- Typhoons induce ground dilatation due to atmospheric pressure drop followed by compression due to rainwater surface loading

Supporting Information:
- Supporting Information S1
- Data Set S1
- Data Set S2

Correspondence to:
M. Mouyen,
maxime.mouyen@univ-rennes1.fr

Citation:
Mouyen, M., Canitano, A., Chao, B. F., Hsu, Y.-J., Steer, P., Longuevergne, L., & Boy, J.-P. (2017). Typhoon-induced ground deformation. *Geophysical Research Letters*, *44*. https://doi.org/10.1002/2017GL075615

Received 8 SEP 2017
Accepted 27 OCT 2017
Accepted article online 2 NOV 2017

Typhoon-Induced Ground Deformation

M. Mouyen[1], A. Canitano[2], B. F. Chao[2], Y.-J. Hsu[2], P. Steer[1], L. Longuevergne[1], and J.-P. Boy[3]

[1]Géosciences Rennes, UMR 6118, OSUR, CNRS, Université Rennes 1, Rennes, France, [2]Institute of Earth Sciences, Academia Sinica, Taipei, Taiwan, [3]EOST-IPGS, UMR 7516, CNRS-Université de Strasbourg, Strasbourg, France

Abstract Geodetic instruments now offer compelling sensitivity, allowing to investigate how solid Earth and surface processes interact. By combining surface air pressure data, nontidal sea level variations model, and rainfall data, we systematically analyze the volumetric deformation of the shallow crust at seven borehole strainmeters in Taiwan induced by 31 tropical cyclones (typhoons) that made landfall to the island from 2004 to 2013. The typhoon's signature consists in a ground dilatation due to air pressure drop, generally followed by a larger ground compression. We show that this compression phase can be mostly explained by the mass loading of rainwater that falls on the ground and concentrates in the valleys towards the strainmeter sensitivity zone. Further, our analysis shows that borehole strainmeters can help quantifying the amount of rainwater accumulating and flowing over a watershed during heavy rainfalls, which is a useful constraint for building hydrological models.

1. Introduction

The solid Earth constantly deforms under the dynamics of its external fluid envelopes, including ocean, continental water, and atmosphere. This is observed in geodetic time series such as very long baseline interferometry (Petrov & Boy, 2004), global navigation satellite system (Argus et al., 2014; Martens et al., 2016), or ground gravimeters (Longuevergne et al., 2009). Surface loads alter the stress tensor in the crust and in turn can lead to strain and potentially to earthquakes. Transient or permanent deformation were observed and modeled to be induced by both solid Earth processes, such as nearby earthquakes (Delescluse et al., 2012; King et al., 1994; Reasenberg & Simpson, 1992; Stein, 1999), slow-slip events (Segall et al., 2006), and surface processes, such as episodic and short-lived events such as hydrologic (Bettinelli et al., 2008) or snow (Heki, 2001) loading, surface erosion (Calais et al., 2010; Steer et al., 2014) and ocean tides (Ide & Tanaka, 2014; Rubinstein et al., 2008; Thomas et al., 2009). The latter examples demonstrate the significant coupling that exists between the Earth fluids envelopes (hydrosphere and atmosphere) and the solid Earth.

Among atmospheric events, tropical cyclones (typhoons) represent good candidates to trigger significative deformation (Hsu et al., 2015; Liu et al., 2009). Indeed, typhoons are localized, extreme climatic events characterized by air pressure drops of several tens of hectopascal (hPa) and, most of the time, heavy rains (Lin & Jeng, 2000). Therefore, air pressure drops, continental rainfalls, and sea level variations represent the most likely sources of surface load changes associated to typhoons. Several typhoons make landfall on Taiwan every year, with an average that increased from 3.3 typhoons per year between 1970 and 1999 to 5.7 between 2000 and 2006 (Tu et al., 2009), 70% of which occurring from July to September. On the other hand, Taiwan is also an active tectonic area. It is located at the junction of the Eurasian and Philippine Sea plates, converging toward each other at a rate of 8 cm yr^{-1} (Yu et al., 1997) with 3 cm yr^{-1} being accommodated by faults on the eastern part of Taiwan (Hsu et al., 2012). A network of borehole strainmeters has been deployed in that region (Figure 1) by the Institute of Earth Sciences, Academia Sinica, in cooperation with the department of Terrestrial Magnetism, Carnegie Institution of Washington, to monitor mainly tectonic deformation (Hsu et al., 2015). Borehole strainmeters record ground deformation with a good precision (1 part per billion = 1 nanostrain, that is, 1 mm of change over 1000 km (Langbein, 2015)) and represent useful tools for studying tectonics and volcanoes (Langbein et al., 1999; Linde et al., 1996; Voight et al., 2006). Recent efforts demonstrate that strainmeters are also effective to monitor hydrology and groundwater extraction (Barbour & Wyatt, 2014). Most of these studies were possible thanks to dense networks of borehole strainmeters operated in the western United States by the U.S. Geological Survey and the University NAVSTAR Consortium Inc., through the Plate Boundary Observatory. For our purpose, since most typhoons initiate in the Pacific Ocean and make first landfall on the eastern coast of Taiwan, the Taiwan strainmeter network

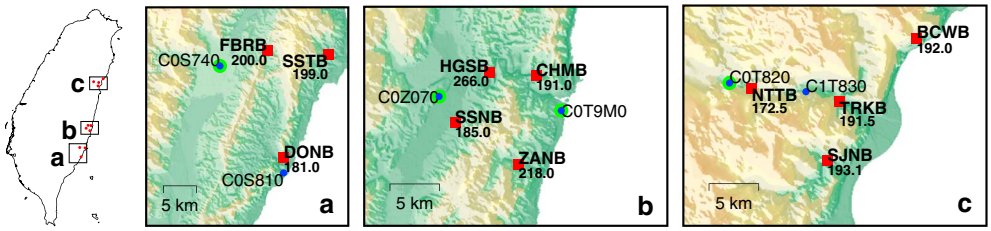

Figure 1. (a–c) Location of the boreholes strainmeters (red squares, with their installation depths in meters), rainfall gauges (blue circles), and barometers (green circles) used in this study, all set on the eastern coast of Taiwan.

provides a unique opportunity to analyze typhoon-induced deformation and to define strategies to properly separate tectonics from surface processes signals.

In this study, we analyze time series recorded by seven borehole strainmeters, for the period ranging from 2004 to 2013, including 31 typhoons. In each case, we use surface air pressure data, nontidal sea level variations model and rainfall data to compute the expected volumetric strain at the depth of the strainmeter sensors and compare them to the actual volumetric strain measured by the strainmeters. Our approach is thus based on the modeling of realistic physical processes, not on the determination of transfer functions between the strain signal and the rainfall or air pressure time series. Our aim is to separate the respective signals induced by atmospheric, oceanic, and rainwater surface loadings on strainmeter records during typhoons and to discuss the potentiality for other processes and contributions.

2. Borehole Strainmeters Data

The strain were measured using Sacks-Everton borehole strainmeters (Sacks et al., 1971) installed along the Longitudinal Valley in eastern Taiwan (Hsu et al., 2015), at depths around 200 m. Their calibration is done by comparing the tidal signals recorded by the strainmeters with computed tidal strain for the location. Although suffering from uncertainties due to inaccurate ocean loading model, topography and nonhomogeneous Earth model parameters, which may eventually bias the interpretation of the strainmeter data (Beaumont & Berger, 1975; Langbein, 2010, 2015), tide calibration remains convenient because tides have large amplitude in the strainmeter records and can be computed using software such as SPOTL (Agnew, 1997, 2012).

To better focus on typhoon-induced processes, we focus on the data recorded during ~10 days centered on the time when typhoons make landfall on Taiwan, or when their paths are the closest to the Taiwanese coasts. We analyze the signal of 31 typhoons from 2004 to 2013. The Taiwan strainmeter network counts 11 instruments today, but due to gaps and network evolution since 2004, we can study the effect of typhoons at up to 7 sites, totaling 72 cases typhoon-induced volumetric deformation (Figure 1). Basic processing consists in removing solid Earth tides and ocean-tidal loading using Baytap08 (Tamura et al., 1991), offsets, and long-term trends.

3. Modeling Typhoon-Induced Deformation

Our hypothesis is that typhoon-induced deformation results from three effects: (1) the change of atmospheric loading due to the drop of surface air pressure; (2) the load of the nontidal oceanic surge, which is also a consequence of air pressure and winds; and (3) the load of rainwater since, in many cases, typhoons are accompanied by heavy rainfalls. Both the atmospheric (1) and nontidal oceanic (2) loadings are computed with volumetric strain Green functions computed with the preliminary reference Earth model (PREM, (Dziewonski & Anderson, 1981)) and calculated for the shallow depths (Kamigaichi, 1998) at which each strainmeter resides.

For effect (1), the Green functions are convolved with global surface air pressure fields provided by the European Centre for Medium-Range Weather Forecasts (ECMWF: ERA-Interim data (Dee et al., 2011)) at 0.25° and 6 h spatial and temporal resolutions. However, the 0.25° spatial resolution is too coarse to properly capture the maximum of surface pressure drop that occurred near the strainmeters. For this reason, when the convolution of the surface pressure field with the Green functions reaches angular distances lesser or equal to

0.1° from the strainmeter, the ECMWF data are replaced by local barometer data provided by the Taiwan Data Bank for Atmospheric & Hydrologic Research service (DBAHR). Following Petrov and Boy (2004), we remove the effect of atmospheric diurnal (S1) and semidiurnal (S2) tides from these air pressure data, using atmospheric S1 and S2 tides models developed by Schindelegger and Ray (2014) on the basis of ground data from the International Surface Pressure Databank (Compo et al., 2011). This model is used as a reference when testing tidal structures in reanalysis products (Díaz-Argandoña et al., 2016). Here correcting the air pressure data with this model reduces by 51% and 78% the spectral amplitude of S1 and S2, respectively.

For effect (2), above oceanic areas, the sea level can accommodate part of the change of air pressure, possibly canceling out any loading effect on the seafloor (inverted barometer hypothesis). These hypothesis and its opposite, the noninverted barometer (all the change of air pressure transmits to the seafloor, as if there were no ocean), were discussed and tested in several studies (Boy et al., 1998; Mémin et al., 2014; van Dam et al., 2012). They agree that the inverted barometer hypothesis is not suitable for air pressure changes at shorter periods than 5 to 20 days, which include typhoons. Therefore, for an optimal evaluation of the non-tidal oceanic effect, we use the modeled dynamic ocean response to air pressure and winds provided by the Toulouse Unstructured Grid Ocean model (TUGO-m (Carrère & Lyard, 2003)) rather than the static inverted-barometer hypothesis. Boy and Lyard (2008) and Boy et al. (2009) have shown the ability of TUGO-m to model sea level variations and its induced geodetic impacts due to storm surges in the North Western European shelf.

Concerning effect (3), it must be emphasized that typhoons also generally lead to heavy rainfall on land. For instance, on 4 August 2009, more than 2000 mm of 3 day cumulated rainfall was recorded in southern Taiwan as typhoon Morakot made landfall (Hong et al., 2010). This rainfall was exceptional, but heavy rains of more than 15 mm h^{-1} remain common during typhoons, and their effect on the strain field is significant compared to the sensitivity of borehole strainmeters (Hsu et al., 2015). However, the processes through which the ground accommodates and discharges this water are various and complex to monitor. It is basically a balance between the ability of the soil and rock in subsurface to split available water into storage, surface runoff, infiltration, and evapotranspiration. Note that the mass of water getting into the air by evapotranspiration becomes part of the atmospheric loading and is therefore accounted for by air pressure measurements.

Comparing the strainmeter signal with the accumulated rain as a function of time shows a good coherence and can be used to assess empirically the transfer function between these two variables (Hsu et al., 2015). Though, the amount of water to include in the loading computation is uncertain. In this study, we suggest that lateral water flow that concentrates water from the watershed toward the sensitivity zone of the strainmeter is a critical process. Since the strainmeters are set in valleys, water is flowing on the topography to accumulate downstream, in addition to the rainwater falling directly above the strainmeters. To model this, we consider a funnel (schematic in Figure S1). The lower (narrower) tip the funnel is a cylinder of accumulated rainwater centered above the borehole strainmeter and whose radius is 3 km. We compute its effect on the volumetric strain at the depth of each strainmeter through the Boussinesq elastic approximation, using PREM's crust Lamé coefficients $\lambda = 3.42\ 10^{10}$ Pa and $\mu = 2.66 \times 10^{10}$ Pa. We use 3 km radius because, given the maximum value of the accumulated rain, the strain effect of the disk load reaches an asymptote, with at most 4% variation for a radius increasing from 3 to 5 km. The volume of this cylinder, hence its loading, has two origins:

1. The rainwater falling directly on the top of this cylinder.
2. The rainwater drained from the sloping sides of the funnel (no strain effect) and delayed by the time it needs to flow from its impact position to the loading cylinder.

The rain time series is taken from the closest rainfall gauge next to each borehole strainmeter (Figure 1). At a given time, the volume of rainwater drained by the funnel depends on its geometry, governed by its upper (wider) radius R_f and its slope α, and by the velocity V of the water flowing on the slopes, which is estimated using the empirical Manning's equation $V = K_s R_h^{2/3} \sqrt{S}$ where R_h is the hydraulic radius, S is the stream gradient, and K_S is the Strickler coefficient, which denotes how easily the water can flow. We set that R_h is equal to the height of rainwater and S to the topographic height gradient ($\tan\alpha$), with $\alpha = 30°$. In this model, we test by trial and error the two parameters R_f and K_S to get the best fitting results between the computed and the observed strain. R_f ranges from 3 (no funnel) to 15 km (with 0.5 km steps) and K_S between 0 (no velocity) and 10 $m^{1/3}\ s^{-1}$ (with 0.5 steps). These two parameters allow to adjust the amplitude and dynamics of the rainwater loading recorded by the strainmeters.

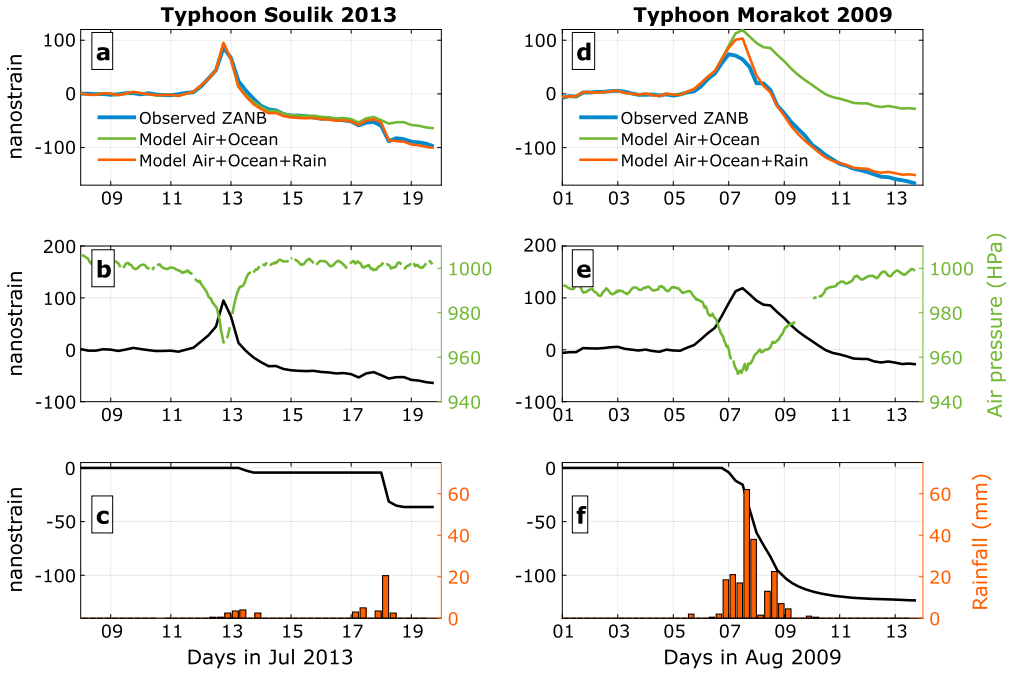

Figure 2. (a) Volumetric strain data at ZANB borehole strainmeter (blue, dilatation is positive, compression is negative) overlaid with computed strain variations considering the air pressure and nontidal ocean loading variations (green line) and the same model to which is added the rainwater loading (red line), during typhoon Soulik, in 2013. (b) Surface air pressure variation (green) and computed volumetric strain effect (black line). (c) Rainfall accumulated every 6 h (red) and volumetric strain effect (black) computed under the Boussinesq elastic approximation. The sum of Figures 2b and 2c strain curves is the red line in Figure 2a. The computed strains were multiplied by the amplitude ratio determined for ZANB (1.9). (d–f) The same as Figures 2a–2c but for the typhoon Morakot in 2009, which brought much heavier rainfalls than Soulik. Air pressure and rainfall data are taken from the weather station C0T9M0 (see Figure 1b for locations).

4. Results

As a first step, to avoid the influence of large hydrological loading on the ground deformation, we focus on "dry" typhoons, i.e., with less than 70 mm of accumulated rainfall from 2 days before to 1 day after the maximum of surface air pressure drop. The main effect at the time of the typhoon is the ground dilatation, itself almost entirely due to the air pressure drop, while the nontidal ocean loading account for less than 1% of the total dilatation. Note that the dilatation of the ground by the ocean loading comes from the use of the shallow depth volumetric strain Green functions, which let loads dilate the ground for some ranges of angular distances. This differs from the effect of loads computed under the Boussinesq elastic approximation, which always generate a ground compression. This was discussed in detail by Kamigaichi (1998), who explained that this property of the Green function is due to the layering of the Earth interior and the Earth surface curvature. But eventually, this has little impact on our computed results.

The fit between observed and computed strain is generally good, especially on the phase of the ground dilatation. However, our computations do not always match the amplitude of the dilation recorded by the strainmeters. We compare the observed and computed volumetric strain stacked either (1) for all the typhoons recorded by each strainmeter or (2) for all the strainmeters recording for each typhoon. The best correlations are found for case (1) with coefficients of determination (R^2) close to one (supporting information Figure S2). This shows that the misfit is strainmeter dependent (rather than typhoon dependent). This is restricted to sites ZANB, HGSB, and TRKB, where the ratio between the observed to computed strain is 1.9 (R^2 = 0.93), 1.8 (R^2 = 0.97), and 0.7 (R^2 = 0.89), respectively. At FBRB, this ratio is almost unity (0.9, R^2 = 0.93). At sites NTTB, CHMB, and SSTB, patterns of underestimation or overestimation between the observed to computed strain ratio are unclear ($R^2 < 0.7$), and we thus prefer to leave it equal to 1. Nonunity ratio may denote calibration errors, which can be up to 30% due to tidal model errors (Langbein, 2010) as well as site effects such as local geology and topography (Berger & Beaumont, 1976), which are not taken into account in our computations. Nevertheless, the good correlation between the observed and computed strain suggests that all

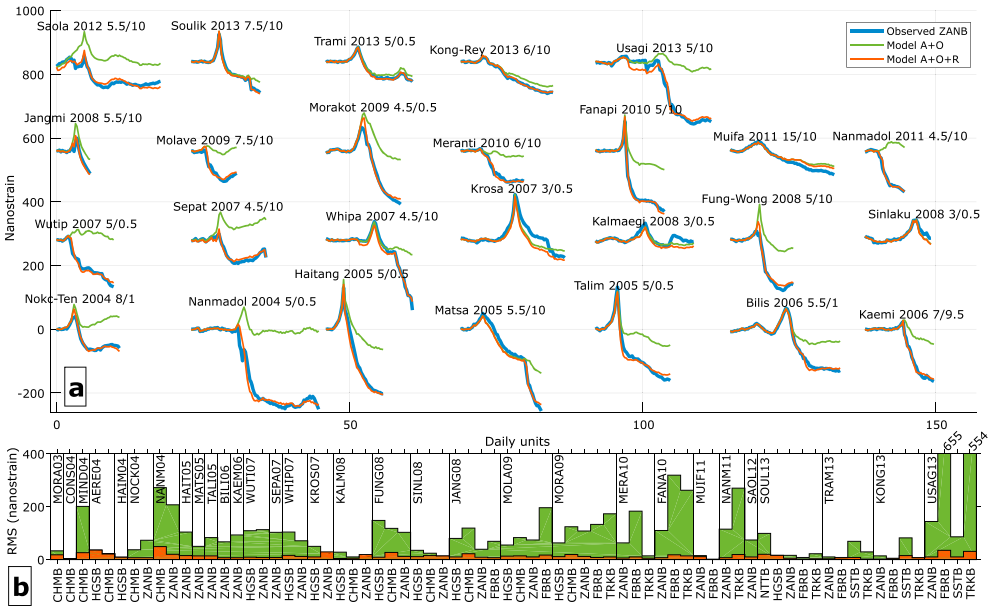

Figure 3. (a) Summary of all the observed (blue) and computed (green and red) strain time series at site ZANB, for typhoons from 2004 to 2013. Model A + O (green) is computed using the air pressure (A) and the non-tidal ocean loading (O) variations. Model A + O + R (red) adds the effect of the rain (R) computed with a funnel model. The text above each comparison plot gives the name of the typhoon, its year, and the set (upper radius of the funnel (in km)/Strickler coefficient) that best explain the strain data. (b) Root-mean-square (RMS) of the residuals between the observed and computed strain time series for A + O (green) and A + O + R (red) models, for all available borehole strainmeters data and typhoons comparisons. Both panels show that the rainwater loading effect properly explains the compression after the typhoon pressure drop.

geophysical sources of deformation are taken into account in the modeling. In the following, the computed strain will be multiplied by this amplitude ratio between observed and computed strain.

We now consider the entire volumetric strain time series, spanning several days before and after the maximum surface air pressure drop, without distinction regarding the amount of rain that accompanies each typhoon. Figure 2 shows typical records of surface air pressure, rainfall, and strain variations for typhoons with little rain (Figures 2a–2c, Soulik, 2013) and heavy rain (Figures 2d–2f, Morakot, 2009) at ZANB site. A common feature across these time series is a ground compression that usually starts in the day following the maximum pressure drop or few hours earlier (Figures 2a–2d). As this compression only occurs when heavy rains are recorded nearby, we argue that it is due to rainwater loading.

Figure 3a shows a complete analysis of all the typhoon-induced strain time series recorded at ZANB (all other strainmeters results in Figure S3) and demonstrate the major influence of rainwater loading on ground deformation. Among the 7 strainmeters sites and the 31 typhoons recorded (Figure 3b), the rainwater concentration model explains strain compression after the typhoon pressure drop. The RMS of the residuals between observed and modeled volumetric strain is systematically reduced, by 81% on average over all typhoons and strainmeters. Table 1 summarizes our results for each borehole strainmeter.

We conclude that every posttyphoon ground compression is explained by rainwater loading, both direct rain above the instrument and indirect rainfall flowing down the watershed topography above each site. This compression is highly site dependent considering the different context of each strainmeter. The simple model accounts for the amplitude increase generated by the accumulation of surface water within the watershed and its concentration toward the strainmeter sensitivity zone, also quantified by the rainfall multiplicative coefficient in Table 1. At sites FBRB and TRKB, this model also explains the time delay between the time of the rain and the time of the ground compression (~19 h for both sites, Figure S4). It corresponds to the time needed for the rainwater. This suggests that these two sites are draining large areas compared to the other sites; thus, rainwater falling afar will eventually need more time to flow toward FBRB and TRKB (we do not consider NTTB and SSTB where just one and three typhoon-induced deformation were measured, hence providing little statistical significance). Indeed, they both have larger watershed areas and R_f than ZANB,

Table 1
Summary of the Main Parameters at Each Borehole Strainmeter

Site	Typhoons observed	Watershed area (km^2)	R_f (km)	K_S	Rainfall multiplicative coefficient	RMS reduction
ZANB	26	12	5.6 ± 2.3	6.0 ± 4.7	4.0 ± 4.5	83%
CHMB	12	8	8.0 ± 3.8	9.2 ± 2.7	7.2 ± 5.4	65%
HGSB	12	9	7.4 ± 4.2	6.9 ± 4.0	3.5 ± 2.8	84%
FBRB	10	15	8.1 ± 3.6	2.9 ± 3.8	6.6 ± 4.3	84%
TRKB	8	26	8.7 ± 3.3	1.9 ± 3.3	6.5 ± 2.6	88%
SSTB	3	14	10.0 ± 5.4	6.8 ± 5.5	13.6 ± 10.5	86%
NTTB	1	13	15.0	1.0	18.1	80%

Note. The rainfall multiplicative coefficient is the ratio between the height of rainwater needed to explain the strain change, that is, the height of rainwater that concentrates at the bottom of the funnel, and the actual rainwater amount measured by local rainfall gauges. The reduction of RMS is computed between the model only accounting for the air pressure change and the model accounting for the air pressure change and the rainwater loading. The drained area is computed from the digital elevation model (DEM, 90 m resolution) of Taiwan using TopoToolbox (Schwanghart & Kuhn, 2010; Schwanghart & Scherler, 2014).

CHMB and HGSB. This is also consistent with the fact that TRKB and FBRB record the largest ground compression during typhoon with heavy rainfalls.

5. Discussion and Concluding Remarks

The strainmeters integrate the loading effect of the rainwater located in the ground above them. At the short time scale considered in this study, a few days, the effect of rainwater is taken as a surface load. Poroelastic processes typically generate amplitude change and time delays with respect to purely elastic deformation (Schuite et al., 2015). Though, in this case, as surface water is involved, the typical time scales required for water infiltration and pressure diffusion in saturated layers would be much longer than a few days observed in this study. Finally, this model considers basic hydrological processes at short term time scales, which are well translated on strainmeters by a purely elastic model. Poroelastic processes can be expected at longer time scales, which are not the scope of this work.

The ground compression due to the rainwater commonly reaches several hundreds of nanostrain with maximum values of ~800 nanostrain at TRKB and FBRB. These amplitudes are comparable with those of local earthquakes (Barbour & Crowell, 2017; Canitano et al., 2015), but coseismic strain changes occurs in a few seconds and can thus be easily distinguished from typhoon-induced deformation, occurring at hourly to daily time scales. However, slow slip earthquakes have both strain amplitudes and time scales (Linde et al., 1996; Peng & Gomberg, 2010; Wang et al., 2008) that could possibly be altered, or even hidden, by rainwater compression signals. In this study, we interpret the entire compression phase of the strain records as a rainwater effect because their respective amplitude and timing agree very well and systematically for many typhoons recorded with several strainmeters. As a result, the suggestion of slow earthquakes triggered by typhoons (Liu et al., 2009) should be evaluated at the light of these new results. Nevertheless, due to the ongoing intensification of landfalling typhoons (Mei & Xie, 2016), the quantitative assessment of their consequences in terms of deformation and stress change in the crust, especially in active tectonics context, remains a justified project. Global Navigation Satellite Systems (GNSS) is also a suitable tool for such a monitoring. The air pressure drop can trigger few mm of vertical displacements and around 1 mm of horizontal displacement. Since GNSS is less sensitive than strainmeters, a strategy would be to stack measurements of a dense array of receivers, to increase the signal-to-noise ratio. Working with subdaily rather than daily solutions should also improve the analysis, because typhoons are rapid events (1–2 days). To finish, the tropospheric delay correction should be carefully computed since typhoon significantly influence it (Chiang et al., 2009). The rainwater loading can also trigger similar or larger displacement, depending on the typhoon considered. In this case, combined horizontal and vertical displacements will provide valuable information on the spatial distribution and the amplitude of the rainwater load (Fu et al., 2013; Wahr et al., 2013).

To conclude, this study clearly demonstrates that large compressional signals in the few days following typhoons can be systematically associated to the effect of rainwater elastic loading. Our simple hydrological model satisfactorily approximates the processes by which rainfalls can flow laterally and concentrate above

strainmeter and deform the ground, both in time and amplitude. It could thus be easily further tested on other borehole strainmeter records located in mountainous areas and help to separate hydrologic and tectonic strain signals. In the meantime, this study also shows that borehole strainmeters are useful tools to quantify the large amount of rainwater brought by typhoons or episodic heavy rainfalls, as well as the time characteristics of lateral water flow and accumulation in valleys. These data are complementary to river discharge and rainfall gauges measurements and may therefore benefit the development of distributed hydrological models.

Acknowledgments
We thank two anonymous reviewers and Editor Andrew V. Newman for their valuable comments. M. M. was supported by an Academia Sinica postdoctoral grant, a Centre National d'Études Spatiales postdoctoral grant, and by the CRITEX project funded by the Agence Nationale pour la Recherche (ANR-11-EQPX-0011). A. C. is supported by an Academia Sinica postdoctoral grant. M. M. and P. S. acknowledge supports from the EROQUAKE project funded by the Agence Nationale pour la Recherche (ANR) and from the France-Taiwan International Associate Laboratory "From Deep Earth to Extreme Events." We thank Osamu Kamigaichi for providing us with his shallow depths strain Green functions. Figure 1 was done with GMT (Wessel & Smith, 1991). The data (strain, local rainfall, and air pressure) for this paper are available as supporting information. Strain data are maintained at http://dmc.earth.sinica.edu.tw/index.php?%20option=com_content&task=view&id=20. This is the contribution of the Institute of Earth Sciences, Academia Sinica, IESAS2165, and the Ministry of Science and Technology grants MOST104-2628-M-001-008-MY4 and MOST105-2811-M-001-031. The authors acknowledge the Taiwan Typhoon and Flood Research Institute, National Applied Research Laboratories, for providing the Data Bank for Atmospheric & Hydrologic Research service (dbahr.narlabs.org.tw). ECMWF ERA-Interim data (global air pressure reanalysis) are available at http://apps.ecmwf.int/datasets/.

References

Agnew, D. C. (1997). NLOADF: A program for computing ocean-tide loading. *Journal of Geophysical Research*, *102*, 5109–5110. https://doi.org/10.1029/96JB03458

Agnew, D. C. (2012). SPOTL: Some programs for ocean-tide loading, SIO Technical Report, Scripps Institution of Oceanography.

Argus, D. F., Fu, Y., & Landerer, F. W. (2014). Seasonal variation in total water storage in California inferred from GPS observations of vertical land motion. *Geophysical Research Letters*, *41*, 1971–1980. https://doi.org/10.1002/2014GL059570

Barbour, A. J., & Crowell, B. W. (2017). Dynamic strains for earthquake source characterization. *Seismological Research Letters*, *88*, 354–370. https://doi.org/10.1785/0220160155

Barbour, A. J., & Wyatt, F. K. (2014). Modeling strain and pore pressure associated with fluid extraction the Pathfinder Ranch experiment. *Journal of Geophysical Research: Solid Earth*, *119*, 5254–5273. https://doi.org/10.1002/2014JB011169

Beaumont, C., & Berger, J. O. N. (1975). An analysis of tidal strain observations from the United States of America: I. The laterally homogeneous tide. *Bulletin of the Seismological Society of America*, *65*(6), 1613–1629.

Berger, J., & Beaumont, C. (1976). An analysis of tidal strain observations from the United States of America II. The inhomogeneous tide. *Bulletin of the Seismological Society of America*, *66*(6), 1821–1846.

Bettinelli, P., Avouac, J. P., Flouzat, M., Bollinger, L., Ramillien, G., Rajaure, S., & Sapkota, S. (2008). Seasonal variations of seismicity and geodetic strain in the Himalaya induced by surface hydrology. *Earth and Planetary Science Letters*, *266*(3–4), 332–3-4, 344. https://doi.org/10.1016/j.epsl.2007.11.021

Boy, J.-P., Hinderer, J., & Gegout, P. (1998). Global atmospheric loading and gravity. *Physics of the Earth and Planetary Interiors*, *109*(3–4), 161–177. https://doi.org/10.1016/S0031-9201(98)00122-8

Boy, J. P., Longuevergne, L., Boudin, F., Jacob, T., Lyard, F., Llubes, M., … Esnoult, M. F. (2009). Modelling atmospheric and induced non-tidal oceanic loading contributions to surface gravity and tilt measurements. *Journal of Geodynamics*, *48*(3–5), 182–188. https://doi.org/10.1016/j.jog.2009.09.022

Boy, J. P., & Lyard, F. (2008). High-frequency non-tidal ocean loading effects on surface gravity measurements. *Geophysical Journal International*, *175*(1), 35–45. https://doi.org/10.1111/j.1365-246X.2008.03895.x

Calais, E., Freed, A. M., Van Arsdale, R., & Stein, S. (2010). Triggering of New Madrid seismicity by late-Pleistocene erosion. *Nature*, *466*(7306), 608–611. https://doi.org/10.1038/nature09258

Canitano, A., Hsu, Y.-J., Lee, H.-M., Linde, A. T., & Sacks, S. (2015). Near-field strain observations of the October 2013 Ruisui, Taiwan, earthquake: Source parameters and limits of very short-term strain detection. *Earth, Planets and Space*, *67*(1), 125. https://doi.org/10.1186/s40623-015-0284-1

Carrère, L., & Lyard, F. (2003). Modeling the barotropic response of the global ocean to atmospheric wind and pressure forcing—Comparisons with observations. *Geophysical Research Letters*, *30*(6). 1275. https://doi.org/10.1029/2002GL016473

Chiang, K. W., Peng, W. C., Yeh, Y. H., & Chen, K. H. (2009). Study of alternative GPS network meteorological sensors in Taiwan: Case studies of the plum rains and typhoon Sinlaku. *Sensors*, *9*(6), 5001–5021. https://doi.org/10.3390/s90605001

Compo, G. P., Whitaker, J. S., Sardeshmukh, P. D., Matsui, N., Allan, R. J., Yin, X., … Worley, S. J. (2011). The twentieth century reanalysis project. *Quarterly Journal of the Royal Meteorological Society*, *137*(654), 1–28. https://doi.org/10.1002/qj.776

Dee, D. P., Uppala, S. M., Simmons, A. J., Berrisford, P., Poli, P., Kobayashi, S., … Vitart, F. (2011). The ERA-Interim reanalysis: Configuration and performance of the data assimilation system. *Quarterly Journal of the Royal Meteorological Society*, *137*(656), 553–597. https://doi.org/10.1002/qj.828

Delescluse, M., Chamot-Rooke, N., Cattin, R., Fleitout, L., Trubienko, O., & Vigny, C. (2012). April 2012 intra-oceanic seismicity off Sumatra boosted by the Banda-Aceh megathrust. *Nature*, *490*(7419), 240–244. https://doi.org/10.1038/nature11520

Díaz-Argandoña, J., Ezcurra, A., Sáenz, J., Ibarra-Berastegi, G., & Errasti, I. (2016). Climatology and temporal evolution of the atmospheric semidiurnal tide in present-day reanalyses. *Journal of Geophysical Research*, *121*, 4614–4626. https://doi.org/10.1002/2015JD024513

Dziewonski, A. M., & Anderson, D. L. (1981). Preliminary reference Earth model. *Physics of the Earth and Planetary Interiors*, *25*(4), 297–356. https://doi.org/10.1016/0031-9201(81)90046-7

Fu, Y., Argus, D. F., Freymueller, J. T., & Heflin, M. B. (2013). Horizontal motion in elastic response to seasonal loading of rain water in the Amazon Basin and monsoon water in Southeast Asia observed by GPS and inferred from GRACE. *Geophysical Research Letters*, *40*, 6048–6053. https://doi.org/10.1002/2013GL058093

Heki, K. (2001). Seasonal modulation of interseismic strain buildup in northeastern Japan driven by snow loads. *Science*, *293*(5527), 89–92. https://doi.org/10.1126/science.1061056

Hong, C.-C., Lee, M.-Y., Hsu, H.-H., & Kuo, J.-L. (2010). Role of submonthly disturbance and 40-50 day ISO on the extreme rainfall event associated with Typhoon Morakot (2009) in Southern Taiwan. *Geophysical Research Letters*, *37*, L08805. https://doi.org/10.1029/2010GL042761

Hsu, Y.-J., Ando, M., Yu, S.-B., & Simons, M. (2012). The potential for a great earthquake along the southernmost Ryukyu subduction zone. *Geophysical Research Letters*, *39*, L14302. https://doi.org/10.1029/2012GL052764

Hsu, Y., Chang, Y., Liu, C., Lee, H., Linde, A. T., Sacks, S. I., … Chen, Y. (2015). Revisiting borehole strain, typhoons, and slow earthquakes using quantitative estimates of precipitation-induced strain changes. *Journal of Geophysical Research: Solid Earth*, *120*, 4556–4571. https://doi.org/10.1002/2014JB011807

Ide, S., & Tanaka, Y. (2014). Controls on plate motion by oscillating tidal stress: Evidence from deep tremors in western Japan. *Geophysical Research Letters*, *41*, 3842–3850. https://doi.org/10.1002/2014GL060035

Kamigaichi, O. (1998). Green functions of the earth at borehole sensor installation depths for surface point load. *Papers in Meteorology and Geophysics*, *48*(4), 89–100. https://doi.org/10.2467/mripapers.48.89

King, G. C. P., Stein, R. S., & Lin, J. (1994). Static stress changes and the triggering of earthquakes. *Bulletin of the Seismological Society of America*, *84*(3), 935–953.

Langbein, J. (2010). Effect of error in theoretical Earth tide on calibration of borehole strainmeters. *Geophysical Research Letters*, *37*, L21303. https://doi.org/10.1029/2010GL044454

Langbein, J. (2015). Borehole strainmeter measurements spanning the 2014 M_w 6.0 South Napa Earthquake, California: The effect from instrument calibration. *Journal of Geophysical Research: Solid Earth*, *120*, 7190–7202. https://doi.org/10.1002/2015JB012278

Langbein, J., Gwyther, R. L., Hart, R. H. G., & Gladwin, M. T. (1999). Slip-rate increase at Parkfield in 1993 detected by high-precision EDM and borehole tensor strainmeters. *Geophysical Research Letters*, *26*, 2529–2532. https://doi.org/10.1029/1999GL900557

Lin, M. L., & Jeng, F. S. (2000). Characteristics of hazards induced by extremely heavy rainfall in Central Taiwan—Typhoon Herb. *Engineering Geology*, *58*(2), 191–207. https://doi.org/10.1016/S0013-7952(00)00058-2

Linde, A. T., Gladwin, M. T., Johnston, M. J. S., Gwyther, R. L., & Bilham, R. G. (1996). A slow earthquake sequence on the San Andreas fault. *Nature*, *383*(6595), 65–68. https://doi.org/10.1038/383065a0

Liu, C. C., Linde, A. T., & Sacks, I. S. (2009). Slow earthquakes triggered by typhoons. *Nature*, *459*(7248), 833–836. https://doi.org/10.1038/nature08042

Longuevergne, L., Boy, J.-P., Florsch, N., Viville, D., Ferhat, G., Ulrich, P., … Hinderer, J. (2009). Local and global hydrological contributions to gravity variations observed in Strasbourg. *Journal of Geodynamics*, *48*(3–5), 189–194. https://doi.org/10.1016/j.jog.2009.09.008

Martens, H. R., Simons, M., Owen, S., & Rivera, L. (2016). Observations of ocean tidal load response in South America from subdaily GPS positions. *Geophysical Journal International*, *205*(3), 1637–1664. https://doi.org/10.1093/gji/ggw087

Mei, W., & Xie, S.-P. (2016). Intensification of landfalling typhoons over the northwest Pacific since the late 1970s. *Nature Geoscience*, *9*(10), 753–757. https://doi.org/10.1038/ngeo2792

Mémin, A., Watson, C., Haigh, I. D., MacPherson, L., & Tregoning, P. (2014). Non-linear motions of Australian geodetic stations induced by non-tidal ocean loading and the passage of tropical cyclones. *Journal of Geodesy*, *88*(10), 927–940. https://doi.org/10.1007/s00190-014-0734-8

Peng, Z., & Gomberg, J. (2010). An integrated perspective of the continuum between earthquakes and slow-slip phenomena. *Nature Geoscience*, *3*(9), 599–607. https://doi.org/10.1038/ngeo940

Petrov, L., & Boy, J.-P. (2004). Study of the atmospheric pressure loading signal in very long baseline interferometry observations. *Journal of Geophysical Research*, *109*, B03405. https://doi.org/10.1029/2003JB002500

Reasenberg, P. A., & Simpson, R. W. (1992). Response of regional seismicity to the static stress change produced by the Loma Prieta earthquake. *Science*, *255*(5052), 1687–1690. https://doi.org/10.1126/science.255.5052.1687

Rubinstein, J. L., La Rocca, M., Vidale, J. E., Creager, K. C., & Wech, A. G. (2008). Tidal modulation of nonvolcanic tremor. *Science*, *319*(5860), 186 LP–186189.

Sacks, I. S., Suyehiro, S., & Evertson, D. W. (1971). Sacks-Evertson Strainmeter, its installation in Japan and some preliminary results concerning strain steps. *Papers in Meteorology and Geophysics*, *22*(3–4), 195–208. https://doi.org/10.2467/mripapers1950.22.3-4_195

Schindelegger, M., & Ray, R. D. (2014). Surface pressure tide climatologies deduced from a quality-controlled network of barometric observations. *Monthly Weather Review*, *142*(12), 4872–4889. https://doi.org/10.1175/MWR-D-14-00217.1

Schuite, J., Longuevergne, L., Bour, O., Boudin, F., Durand, S., & Lavenant, N. (2015). Inferring field-scale properties of a fractured aquifer from ground surface deformation during a well test. *Geophysical Research Letters*, *42*, 10,696–10,703. https://doi.org/10.1002/2015GL066387

Schwanghart, W., & Kuhn, N. J. (2010). TopoToolbox: A set of Matlab functions for topographic analysis. *Environmental Modelling and Software*, *25*(6), 770–781. https://doi.org/10.1016/j.envsoft.2009.12.002

Schwanghart, W., & Scherler, D. (2014). Short communication: TopoToolbox 2—MATLAB-based software for topographic analysis and modeling in Earth surface sciences. *Earth Surface Dynamics*, *2*(1), 1–7. https://doi.org/10.5194/esurf-2-1-2014

Segall, P., Desmarais, E. K., Shelly, D., Miklius, A., & Cervelli, P. (2006). Earthquakes triggered by silent slip events on Kilauea volcano, Hawaii. *Nature*, *442*(7098), 71–74. https://doi.org/10.1038/nature04938

Steer, P., Simoes, M., Cattin, R., & Shyu, J. B. H. (2014). Erosion influences the seismicity of active thrust faults. *Nature Communications*, *5*, 5564. https://doi.org/10.1038/ncomms6564

Stein, R. S. (1999). The role of stress transfer in earthquake occurrence. *Nature*, *402*(6762), 605–609. https://doi.org/10.1038/45144

Tamura, Y., Sato, T., Ooe, M., & Ishiguro, M. (1991). A procedure for tidal analysis with a Bayesian information criterion. *Geophysical Journal International*, *104*(3), 507–516. https://doi.org/10.1111/j.1365-246X.1991.tb05697.x

Thomas, A. M., Nadeau, R. M., & Bürgmann, R. (2009). Tremor-tide correlations and near-lithostatic pore pressure on the deep San Andreas fault. *Nature*, *462*(7276), 1048–1051. https://doi.org/10.1038/nature08654

Tu, J. T., Chou, C., & Chu, P. S. (2009). The abrupt shift of typhoon activity in the vicinity of Taiwan and its association with western North Pacific-East Asian climate change. *Journal of Climate*, *22*(13), 3617–3628. https://doi.org/10.1175/2009JCLI2411.1

van Dam, T., Collilieux, X., Wuite, J., Altamimi, Z., & Ray, J. (2012). Nontidal ocean loading: Amplitudes and potential effects in GPS height time series. *Journal of Geodesy*, *86*(11), 1043–1057. https://doi.org/10.1007/s00190-012-0564-5

Voight, B., Linde, A. T., Sacks, I. S., Mattioli, G. S., Sparks, R. S. J., Elsworth, D., … Williams, P. (2006). Unprecedented pressure increase in deep magma reservoir triggered by lava-dome collapse. *Geophysical Research Letters*, *33*, L03312. https://doi.org/10.1029/2005GL024870

Wahr, J., Khan, S. A., Van Dam, T., Liu, L., Van Angelen, J. H., Van Den Broeke, M. R., & Meertens, C. M. (2013). The use of GPS horizontals for loading studies, with applications to northern California and southeast Greenland. *Journal of Geophysical Research: Solid Earth*, *118*, 1795–1806. https://doi.org/10.1002/jgrb.50104

Wang, K., Dragert, H., Kao, H., & Roeloffs, E. (2008). Characterizing an "uncharacteristics" ETS event in northern Cascadia. *Geophysical Research Letters*, *35*, L15303. https://doi.org/10.1029/2008GL034415

Wessel, P., & Smith, W. H. F. (1991). Free software helps map and display data. *Eos, Transactions*, *72*, 445–446.

Yu, S.-B. B., Chen, H.-Y. Y., & Kuo, L.-C. C. (1997). Velocity field of GPS stations in the Taiwan area. *Tectonophysics*, *274*(1–3), 41–59. https://doi.org/10.1016/S0040-1951(96)00297-1